IAEA nuclear fusion

PAPER • OPEN ACCESS

Absolute measurement of the deuterium–tritium reaction gamma-ray emission in magnetic confinement fusion plasmas

To cite this article: Giulia Marcer *et al* 2025 *Nucl. Fusion* **65** 086036

OPEN ACCESS
IOP Publishing | International Atomic Energy Agency Nuclear Fusion
Nucl. Fusion **65** (2025) 086036 (12pp) https://doi.org/10.1088/1741-4326/adeea7

Absolute measurement of the deuterium–tritium reaction gamma-ray emission in magnetic confinement fusion plasmas

Giulia Marcer[1,2], Andrea Dal Molin[1,*], Massimo Nocente[2], Marica Rebai[1], Davide Rigamonti[1], Maurizio Angelone[3], Angela Bracco[4], Franco Camera[4], Carlo Cazzaniga[5], Teddy Craciunescu[6], Gabriele Croci[1,2], Marco Dalla Rosa[2], Simone Lorenzo Fugazza[2], Luca Giacomelli[7], Giuseppe Gorini[2], Yevgen Kazakov[8], Evgeniy Khilkevitch[9], Andrea Muraro[1], Enrico Panontin[10], Enrico Perelli Cippo[1], Mario Pillon[11], Oscar Putignano[1], Jimmy Scionti[1], Alexander Shevelev[9], Marco Tardocchi[1], the EUROfusion Tokamak Exploitation Team[a] and JET Contributors[b]

[1] Institute for Plasma Science and Technology, Consiglio Nazionale delle Ricerche, Milan, Italy
[2] Department of Physics, University of Milano-Bicocca, Milan, Italy
[3] Department of Industrial Engineering, University of Rome Tor Vergata, Rome, Italy
[4] Department of Physics, University of Milan, Milan, Italy
[5] ISIS Facility, UKRI-STFC, Rutherford Appleton Laboratory, Didcot, United Kingdom of Great Britain and Northern Ireland
[6] National Institute for Laser, Plasma and Radiation Physics, Bucharest, Romania
[7] European Commission—Joint Research Centre, Ispra, Italy
[8] Laboratory for Plasma Physics, LPP-ERM/KMS, TEC Partner, Brussels, Belgium
[9] Scientist from St. Petersburg, Russian Federation
[10] Plasma Science and Fusion Center, Massachusetts Institute of Technology, Cambridge, MA, United States of America
[11] Nuclear Department, ENEA, Frascati, Italy

E-mail: andrea.dalmolin@istp.cnr.it

Received 20 January 2025, revised 20 May 2025
Accepted for publication 11 July 2025
Published 24 July 2025

Abstract
The Joint European Torus performed its second deuterium–tritium (DT) campaign at the end of 2021. This unique opportunity was exploited to carry out the first absolute measurement in a magnetic confinement plasma of the total gamma-ray emission from the DT fusion reaction, namely the less probable (branching ratio $= 2.4 \cdot 10^{-5}$) electromagnetic counterpart of the main neutronic decay channel. A single line of sight gamma-ray spectrometer was employed for this purpose. Numerous challenges had to be addressed in order to pursue the goal: (1) characterise the detector beamline and its detection efficiency in absolute terms, (2) dealing with an extended

[a] See Joffrin *et al* 2024 (https://doi.org/10.1088/1741-4326/ad2be4) for the EUROfusion Tokamak Exploitation Team.
[b] See Maggi *et al* 2024 (https://doi.org/10.1088/1741-4326/ad3e16) for JET Contributors.
[*] Author to whom any correspondence should be addressed.

and non-uniform source, (3) suppress the intense neutron background, (4) handle the high event rate at the detector and (5) discriminate between signal and background in the acquired energy spectrum. This paper describes the procedure adopted for measuring the total DT gamma-ray yield of 96 DT plasma discharges with event rates below hundred kHz. The results were validated through a comparison with the neutron yields provided by the Joint European Torus neutron monitors, revealing an outstanding 0.983 linear correlation. This work proves the feasibility to employ the gamma-ray emission of the DT fusion reaction as a secondary indicator for measuring the fusion power in magnetically confined DT plasmas.

Keywords: deuterium–tritium reaction, fusion power, gamma-ray spectroscopy

(Some figures may appear in colour only in the online journal)

1. Introduction

In the next decades, the main progress toward electricity production from nuclear fusion will be led by magnetic confinement fusion devices like the tokamaks ITER [1, 2] and SPARC [3]. Due to its higher probability to occur at lower temperatures [4], deuterium and tritium (DT) is selected as the best fuel mixture to pursue this goal in such magnetic devices.

The fusion yield is the total number of DT reactions obtained during a plasma discharge and is a key performance metric for current and future tokamaks. Presently, concerning magnetic confinement fusion devices, the only direct technique available for measuring the fusion yield relies on absolutely counting the 14 MeV neutrons produced by the D(T, ^{4}He)n reactions. This standard technique is based on the combined use of activation foils and fission chambers and requires extensive in-situ calibration campaigns together with detailed numerical Monte Carlo (MC) simulation of the entire reactor [5–14]. Since neutrons can frequently interact with the environmental materials before being detected, changes around the device affect the neutron signal, making it necessary to repeat the calibration campaign after any environment variation.

According to the ITER nuclear regulator, two independent methods are required for assessing the fusion power for safety reasons.

In a DT fusion nuclear reaction, deuterium and tritium generate a ^{5}He nucleus in its second excited state, which predominantly decays from the resonance level ($J^\pi = 3/2^+$) to the ground state of a ^{4}He nucleus through the emission of the well-known 14.1 MeV neutron. Alternatively, as shown in figure 1, ^{5}He can decay radiatively to its own ground state ($J^\pi = 3/2^-$) or to its first excited state ($J^\pi = 1/2^-$). In the former case, a 16.7 MeV gamma-ray (γ_0 from now on) is produced while, in the latter, a 12.5 MeV gamma-ray (γ_1) is emitted before the nucleus de-excites non-radiatively to the ground state:

$$\begin{aligned} {}^2\mathrm{H} + {}^3\mathrm{H} \rightarrow {}^5\mathrm{He}^{**} &\rightarrow {}^4\mathrm{He} + \mathrm{n} \\ &\rightarrow {}^5\mathrm{He} + \gamma_0 \\ &\rightarrow {}^5\mathrm{He}^{*} + \gamma_1 . \end{aligned}$$

The absolute measurement of these radiative branches emission could be used as a second direct method to measure the fusion power. The limited amount of interaction channels by which gamma-rays interact with matter, in fact, make the absolute calibration of gamma-ray measurements easier and less dependent on the tokamak environment.

While the neutron emitting branch has an almost unitary probability to occur, though, the branching ratio of the two radiative channels is poorly known, thus preventing their deployment as a mean for fusion power determination.

In the last half century, tens of attempts were conducted to ascertain this value both in accelerator facilities or in inertial confinement fusion experiments [15–22]. The measured values vary within a factor of twenty, from $1.27 \cdot 10^{-5}$ up to $2.84 \cdot 10^{-4}$, at least proving that the neutron branch is by far the most probable channel. These large discrepancies are likely due to difficulties in measuring this emission caused by both the unavoidable intense 14 MeV neutron induced background often overwhelming the weak gamma-ray signal and the broad shape of the gamma emission lines, due to the large intrinsic widths of the ^{5}He lower energy levels, which can also be interpreted as continuum for the α + n nuclear system [23, 24].

This paper describes the first absolute measurement of the total DT gamma-ray yield in a magnetic confined fusion plasma carried out in 2021, which also led to the first measurement of the DT gamma-to-neutron branching ratio ($2.4(5) \cdot 10^{-5}$) in the same environment. The higher reliability of this measurement with respect to previous assessments of the reaction branching ratio is discussed in the related articles [26, 27].

At the time this experiment was conducted, due to the complexity of handling tritium, the Joint European Torus (JET) was the only tokamak capable of operating with tritium as fuel and was carrying out the second DT experimental campaign, the DTE2 [28, 29]. The aim of this work was to measure the total DT gamma-ray emission during the JET DT discharges and proving that this absolute measurement can be used to infer the fusion yield. JET was already equipped with a single line of sight (LoS) gamma-ray spectrometer designed for fast ions measurements [30–32] which was used for this purpose.

For each discharge, the core principle adopted to measure the total gamma-ray yield Y relied on the analysis of the detector pulse height spectrum (PHS) and the plasma emission profile based on the formula:

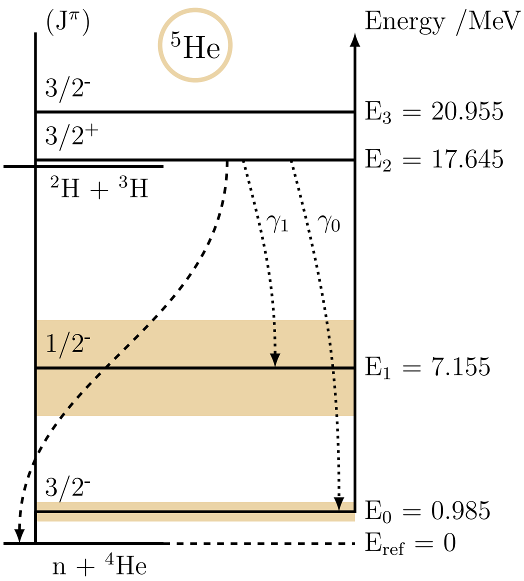

Figure 1. First energy levels of the ^{5}He nucleus and its associated decay scheme from the second excited state (dotted lines represent the two γ_0 and γ_1 radiative transitions). Energy levels are referred to the n + ^{4} He state. Data are taken from [25], table 5.2.

$$YTA\varepsilon = Cf \quad \rightarrow \quad Y = \frac{Cf}{TA\varepsilon}$$

where:

- T is the transport factor, which takes into account both the non-uniform plasma volumetric emission and the gamma-rays optical transport toward the detector. It was determined with MC simulations, semi-analytical codes and plasma emission profile information derived from the JET neutron camera,
- A is the gamma-ray transmission factor through collimators and attenuators, the most important of which is a neutron attenuator located in front of the detector to suppress the intense neutron background,
- ε is the detector gamma-ray detection efficiency, which was determined with a novel technique based on the specific detector employed for this purpose,
- C is the integrated number of counts in the PHS in an optimised energy range defined as the region of interest (RoI),
- f is the fraction of DT gamma-ray events in the RoI.

Each of these five factors was carefully determined as described in the next sections, which are organised as follows. The experiment is presented in section 2, the acquisition of the PHS and its integration C in the RoI are discussed in section 3, the determination of f is explained in section 4 while T, A and ε are treated in section 5. The results and their validation follow in section 6 together with the discussion in section 7, before terminating with the conclusions in section 8.

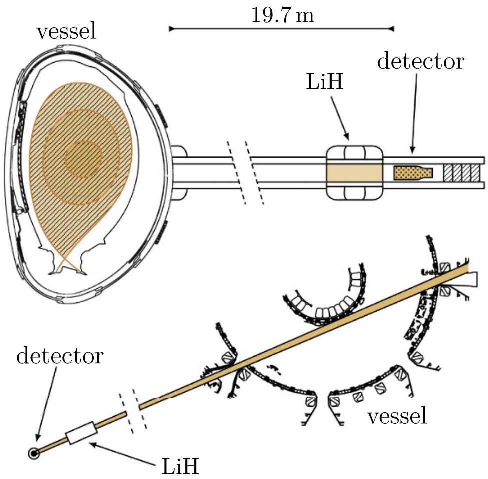

Figure 2. Schematic representation of the tangential gamma-ray spectrometer line of sight geometry in the JET tokamak. The poloidal cross section is presented in the top portion of the figure, while a top-down view of the line of sight is shown in the bottom half.

2. The experiment

During the DTE2, record fusion rates were achieved up to 4–5 $\cdot 10^{18}$ neutrons per second [33] and experiments were carried out on different research topics.

Among other diagnostics, JET was equipped with three cerium-doped lanthanum bromide ($LaBr_3$) gamma-ray spectrometers to measure gamma-ray spectra above 1 MeV for energetic ions studies [34]. Because of the advantages related to its LoS geometry, the diagnostic selected to measure the JET DT gamma-ray yield was the tangential gamma-ray spectrometer (TGRS). A tangential LoS, in fact, crosses the plasma center twice and is less dependent on changes in the peripheral area of the vessel with respect to a radial or vertical LoS.

This instrument consists of a cylindrical 3 $\times$ 6 inches $LaBr_3$ crystal coupled to a R10233 Hamamatsu PhotoMultiplier-Tube (PMT) with 3.5 inch diameter, provided with an active voltage divider for high energy and high counting rate measurements in the range of MHz [30, 35]. The TGRS is located about 20 m outside the vessel (as schematically shown in figure 2), at the end of a horizontal, collimated LoS lying in the equatorial plane, tangent to the inner vessel walls. Several elements contribute to collimate the gamma-rays: the main contribution, starting from the plasma, comes from the vessel port, the beamline cylindrical inconel supporting structure, two cylindrical lead collimators and a rectangular hole in the concrete bioshield. The LoS has a cross sectional area of about 300 cm^2 at the tangent point with the inner vessel.

The other crystals [36] had a vertical LoS entering the plasma vessel from above, shared with other diagnostics with relative collimators and attenuators which would have tampered the absolute measurements. Furthermore, unlike the

Table 1. Used JET plasma discharges from the DTE2 divided into sets depending on their JET pulse numbers (JPN, first column), the fuel tritium percentage T is given in the second column, the third and the last columns contain the average neutron rate R_n and total neutron yield Y_n in each set.

JPNs	T (%)	R_n /10^{15}/s	Y_n /10^{16}
99554-99 567	2.21	7.59	7.53
99571-99 580	1.54	3.60	5.40
99581-99 591	1.31	3.43	3.65
99655-99 677	4.45	5.01	5.90
99680-99 688	2.86	4.72	7.09
99696-99 744	1.97	4.92	7.39

TGRS, their acquisition systems were not optimised for the DT gamma-ray measurement (section 3).

Cerium-doped $LaBr_3$ crystals represent the state-of-the-art of the scintillators technology for gamma-ray spectroscopy: they feature the best energy resolution (<2.9% at 662 keV), a short decaying time (<30 ns) and high light yield (63 photons/keV) [37, 38]. Though, they manifest an intrinsic activity due to the ^{138}La isotope and unavoidable actinide impurities which covers an energy range up to 3 MeV. At JET, because of its moderate rate (about 700 events per second), this natural activity did not represent a concern with respect to the signal coming from the plasma. On the other hand, as explained in section 4, the crystal detection efficiency to gamma-rays (ε) was determined with a novel technique purposely developed for this work which exploits exactly the $LaBr_3$ intrinsic activity [39].

$LaBr_3$ crystals have an almost unitary efficiency both to 14 MeV neutrons and 17 MeV gamma-rays [40]. Given that the gamma-to-neutron branching ratio is small, the gamma-ray signal would have been overwhelmed by a neutron induced background at least four orders of magnitude larger. If no attenuation were used, based on simulations and previous experimental campaigns, the neutron flux expected at the detector would have been about 10^{10} events per second. Given that a single event generates a waveform of about 200 ns in the TGRS output signal, the expected event rate could have been too high to allow for the identification of individual events and perform absolute counting of the DT gamma-ray emission. Therefore, it was mandatory to locate a neutron attenuator in front of the detector.

Due to its properties, which are discussed in section 3, this problem was addressed by installing a 93 cm long lithium hydride (LiH) [41] attenuator inside the beamline, in front of the detector. Though, because of an other source of background which will be discussed in section 3, a large number of plasma discharges presented excessive event rates making it necessary to perform a selection on the usable plasma pulses. Table 1 shows the list of the used discharges along with information on the neutron yields and tritium concentration associated to them.

As the measurement validation is concerned, the relationship between the DT gamma-ray and the 14 MeV neutron yields was exploited.

In 2021, JET was the only tokamak equipped with neutron monitors capable of assessing the total 14 MeV neutron yield through this standard technique providing a nominal 7% uncertainty. These neutron yields were used to validate the measured fusion power based on the gamma-ray measurement. A linear correlation between the discharges gamma-ray yield and neutron yield was expected in case of success of the experiment, with the line slope corresponding to the gamma-to-neutron branching ratio [26].

3. Spectrum acquisition

At JET, the neutrons produced inside the plasma and interacting with the vessel walls produce a large number of gamma-rays usually referred to as prompt-gammas. Being gamma-rays, they travel across the neutron attenuator with small intensity reduction and are finally detected by the TGRS as well, resulting in an intense background in the spectrum which covers energies up to about 10 MeV. Compared to the fusion gamma-ray signal, on average, it was measured to be 10^3 times more intense. This source of background limited the range of DTE2 discharges for which high energy gamma-ray measurements were possible.

The event rate at the detector for the selected discharges was below 100 kHz. A standard trigger-based electronic instrumentation, as the one conventionally adopted for gamma-ray spectroscopy, would have led to an unacceptably loss or miss-parsing of events due to dead time and pile-up, rendering the absolute measurement of gamma-ray yield impossible. This problem was addressed by upgrading the spectrometer digitiser with a National Instruments, model NI5772, module PXIe-7976 FlexRIO, previously used for runaway electron measurements by bremsstrahlung emission at ASDEX Upgrade [42]. This system enabled continuous digitisation throughout the discharge, eliminating dead-time issues typical of trigger-based acquisition systems and allowing for off-line parsing of the piled-up events. A moderate sampling frequency of 200 MHz was used to manage the large data amount per discharge still allowing for a reliable data processing.

As highlighted in figure 3(which shows the sum of all acquired spectra), the fusion gamma-rays are among the most energetic particles emitted by the plasma, mainly covering the upper part of the spectrum between 12 and 17 MeV. The latter was selected as the RoI for the counts integration C. According to the performed MCNP [43] simulations (section 5.3), in fact, at such high energies the scattered gamma-rays are negligible compared to the direct ones (<1%), making the measurement even less dependent on the tokamak environment.

The energetic side of the spectrum, though, is the one which mostly suffers from distortions due to pile-up effect. The signal identification therefore heavily depends on the pile-up identification capabilities.

The spectrometer data were analysed with a Python program [44, 45] based a on dedicated pile-up recovery algorithm. The program determines the gates containing pulses with the time-over-threshold technique, where the

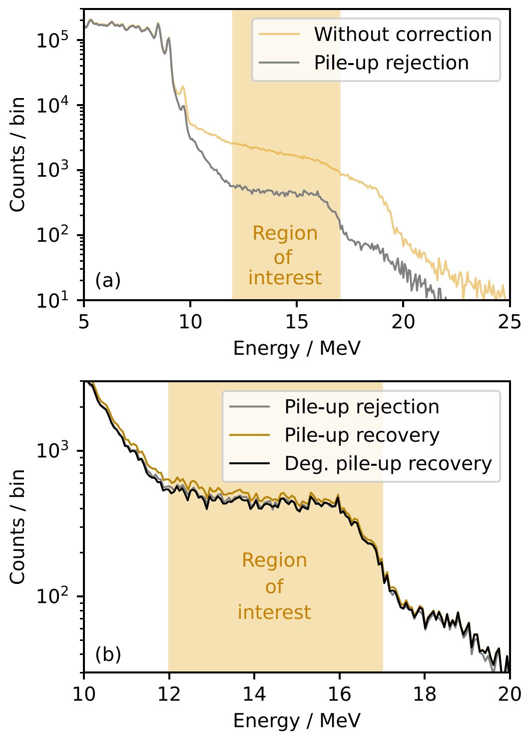

Figure 3. Zoom on the high energy range of the sum spectrum of all analysed plasma pulses. The spectrum is shown without any pile-up correction (orange line) and with pile-up rejection (gray line) in the plot above, between 5 and 25 MeV. The plot below shows again the spectrum with pile-up regection (gray line) together with the spectrum with non-degenerate pile-up correction (brown line) and with degenerate pile-up correction (black line) in the plot below, between 10 and 20 MeV.

threshold was customly defined based on the instrumental noise. Piled-up events are identified in gates that last longer than the standard duration of a single pulse.

The code can run in pile-up rejection mode, leading to the gray curve shown in figure 3. When the rejection mode is on, pile-up gates are simply discarded and only non-pile-up events are used to populate the spectrum. The rejection of piled-up events made it possible to recover the proper spectral shape of the high energy side of the spectrum, as shown in the figure (subplot a), leading to a signal shape compatible to the one expected from theory.

Since an absolute measurement had to be performed, though, the absolute number of events at the detector was needed. Therefore, it was necessary to recover the piled-up events by means of a piled-up recovery algorithm. When the code is run in pile-up recovery mode, individual events are detected by their inflection points, after having evaluated the signal numerical second order derivative. Then, single events are resolved as a linear sum of scaled reference pulses (brown curve in the figure, subplot b). In the sum spectrum shown in figure 3, pile-up recovery allowed to increase by 8.35% the events in the ROI with respect to pile-up rejection.

Numerical benchmarking showed that the maximum counting rate for the pile-up recovery algorithm is 2 MHz, if a 5% failure is accepted, which was more than 40 times the rate of the parsed plasma discharges.

When the events are closer than ∼35 ns, though, the pile-up correction algorithm can be unable to correct or even identify the occurrence of pile-up, leading to what is known as the degenerate pile-up effect. In order to correct for this effect, a further algorithm was developed and implemented in Python [46]. The algorithm is directly applied to the PHS and corrects for the degenerate pile-up distortion based only on the spectrum acquisition time and two assumptions: (1) the events follow a Poisson distribution, (2) each time two events overlap, they result in the spectrum as a single event having as amplitude the sum of the overlapping pulses amplitudes.

In the sum spectrum shown in figure 3, the degenerate pile-up correction lowered the events in the ROI by 9.98% with respect to the pile-up recovery events, thus getting very close to the pile-up rejection spectrum.

The two pile-up handling codes were tested both on real and synthetic data, resulting capable to provide reliable results within the rates of the parsed discharges data.

Another problem which had to be dealt with while working with high fluxes at the detector was the drift of the PMT gain. PMT gain-drift is a well-known source of uncertainty in measurements at high counting rates. An active base was installed to help with this problem. During the DTE2, though, such intense event rates caused significant reductions (up to 10% at some hundreds kHz) in the PMT gain despite the active base, producing heavy spectral degradation if no countermeasures were taken.

The problem was addressed by placing a light emitting diode (LED) pointing direct to the PMT photocathode. The LED was operated to generate reference light pulsed with a fixed frequency of 10 kHz and an equivalent energy of 9.25 MeV [42].

Based on the LED pulses periodic occurrence, they were identified and used to monitor the PMT gain fluctuations allowing to correct for its drift. An example of drift correction is shown in figure 4. After gain drift correction, the LED pulses were eventually removed from the spectra.

Once all spectra were corrected for pile-up and PMT gain-drift related effects, the number of integrated events C was computed as the sum of the bin entries in the PHS between 12 and 17 MeV. The uncertainties associated to C were both statistical and due to the degenerate pile-up correction, as described in the related paper [46].

4. Spectrum analysis

The acquired spectrum was energy-calibrated using four prompt-gammas lines emitted from neutrons interactions with nickel and chromium, which were present in the alloys composing the vacuum vessel and some structures along the detector beamline. Namely:

- inelastic scattering with ^{58}Ni (1.454 MeV),
- capture by ^{58}Ni (8.53 MeV),

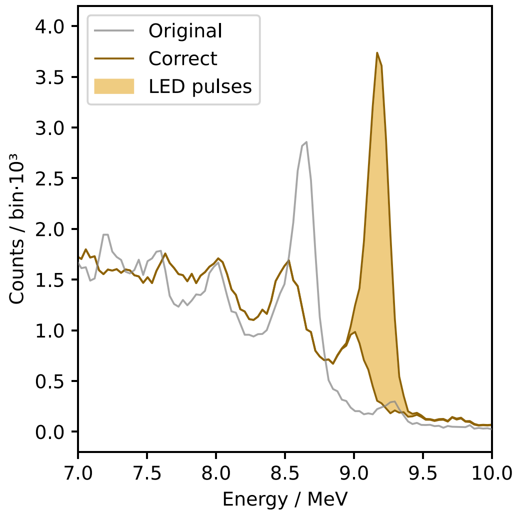

Figure 4. Example of photomultiplier-tube gain-drift correction on JPN 99 608, between seconds 46 and 48. Zoom in the energy region around the LED pulses, which were finally removed from the spectrum.

- capture by ^{58}Ni (8.998 MeV),
- capture by ^{53}Cr (9.719 MeV).

These structures were fitted as Gaussian functions with a linear background and their centroid parameters used as the peaks positions.

In order to take into account the non linearity of the acquisition response and to improve the calibration reliability in the high energy range, the γ_0 emission was used too to perform a quadratic calibration. Its expected signal shape was used for the fit to extrapolate its channel position. Given the low signal-to-noise ratio of most of the discharges in the RoI, though, this calibration could be performed only on the sum-spectrum of all PHS once they were linearly calibrated using the prompt-gammas lines. A small quadratic term of about 10^{-5} was found, corresponding to an upward scaling of the energies approximately equal to 1.5% at 17 MeV. Each single PHS was then quadratically-calibrated according to this result.

Throughout the energetic calibration of the spectra, it was possible to neglect the thermal and beam-plasma shift of the source energy (10 keV and $\sim$100 keV), being smaller than a single PHS bin width (approximately 250 keV). Figure 5 shows the quadratic calibration performed on the sum-spectrum, highlighting all the used lines and structures.

All events in the spectrum RoI can be attributed to either the signal (γ_0 or γ_1 transitions) or the background components. It is crucial for the determination of the DT gamma-ray yield to attribute the intensities of these components accurately. Given the broad spectral shape of the two radiative transitions, particular care had to be taken into their description to allow for discrimination from the background.

The spectral shape of γ_0 and γ_1 transitions were computed using the R-matrix technique [47] with the properties of the ^{5}He energy levels presented in table 5.2 of [25]. The resulting spectral shapes were convolved with the detector response function computed using MCNP, obtaining the curves shown

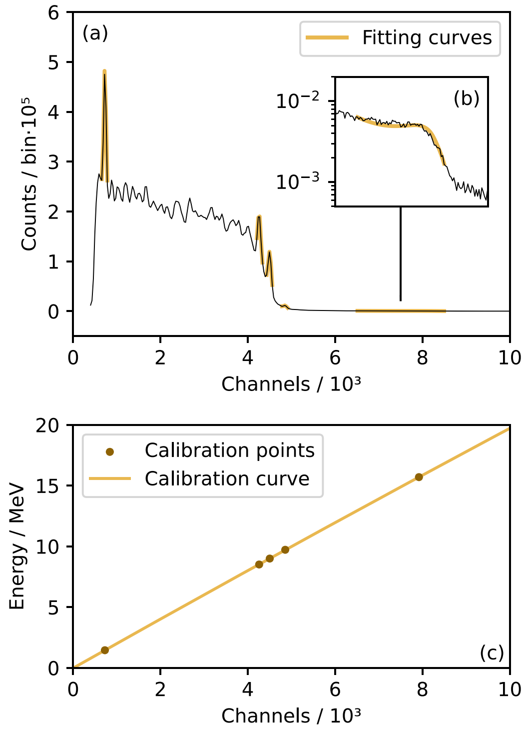

Figure 5. Energy calibration of the sum-spectrum. Pulse height spectrum in the plot (*a*) with a zoom on the fusion peak in the insert (*b*), in logarithmic scale. The Gaussian calibration curves are plotted as thick orange lines. The quadratic calibration curve is shown in the subplot (*c*).

in figure 6. The full-energy peak and escape peaks do significantly overlap, as the γ_0 and γ_1 emission spectra were already too broad even before accounting for the instrumental response [27]. The detector response was also broadened with a Gaussian function whose width parameter was taken equal to 150 keV at 16.7 MeV, according to the detector energy resolution, extrapolated from the calibration points Gaussians widths. Simulations were also performed independently with the GEANT 4 platform [48], providing compatible results within 1%.

All possible detection processes which include, beside the full-energy deposition, also the single and double escape peaks and the Compton contribute to broaden the measured spectral shape of γ_0 and γ_1, as shown in figure 6.

Regarding the background components, a first principle description was not possible. Contributions due to concurrent fusion reactions in the RoI from radiative decays such as pT, DD, D^{3}He or T^{3}He were all excluded either by the expected spectral shape or due to their expected negligible yields [25]. Radiative emissions from nuclear reactions between the 14 MeV neutrons and the LoS materials are the suspected cause of most of the background. Unfortunately, the cross-sections of these reactions are either unknown or known with significant error bars for a detailed identification of the individual processes contributing to the background.

This uncertainty prevented the identification of individual contributions in the background, which was therefore modelled using a combination of an exponential and a polynomial

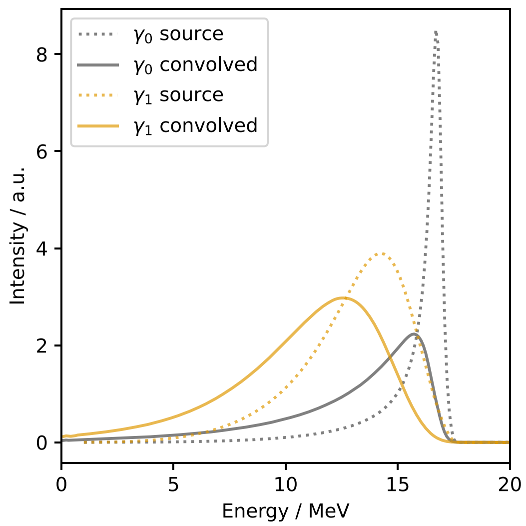

Figure 6. Spectral shapes of γ_0 and γ_1 sources as predicted according to the R-matrix technique [47] with the energy levels given in [25] are shown (in dotted lines) together with their convolution with the detector response function (solid lines).

function. The analysis was performed on the sum-spectrum data, in order to reduce the statistical deviations. Polynomials of different degrees were investigated creating a set of possible models to be fitted to data:

$$f_n(E,\vec{p}) = p_0 S_0(E) + p_1 S_1(E) + p_2 \exp(-E/p_3) + \sum_{i=0}^{n} p_{i+4} E^i$$

where:

- E is the energy,
- $\vec{p}$ is the vector containing all free parameters (the number of free parameters is equal to $n+4$ where n is the degree of the polynomial).
- S_0 and S_1 are the γ_0 and γ_1 spectral shapes.

These models were fitted to the data in the energy region between 10 MeV and 20 MeV to best capture the exponential behaviour (that is predominant at the lower energy range) and the polynomial behaviour present at the high end of the range. The fits of the different f_n models were compared using the corrected Akaike information criterion (AICc) [49]. The f_2 was found to be the best model with an AICc = 51.82.

According to the fit results (figure 7), in the region between 12 MeV and 17 MeV (which turned out to be the region with the best signal-to-background ratio), the counts were attributed as follows: $f_0 = 43.3(10)\%$ to the γ_0 transition, $f_1 = 24.1(50)\%$ to the γ_1 transition and the remaining 32.6% to the background components. As can be observed, the fraction f_1 of γ_1 events is affected by a 20.7% uncertainty, finally resulting in the leading source of uncertainty on the total gamma-ray yields.

With these factors, it was possible to compute the absolute number of γ_0 and γ_1 signal events at the detector. In the section 6 section, these events will be referred to as $C_0 = C \cdot f_0$ and $C_1 = C \cdot f_1$.

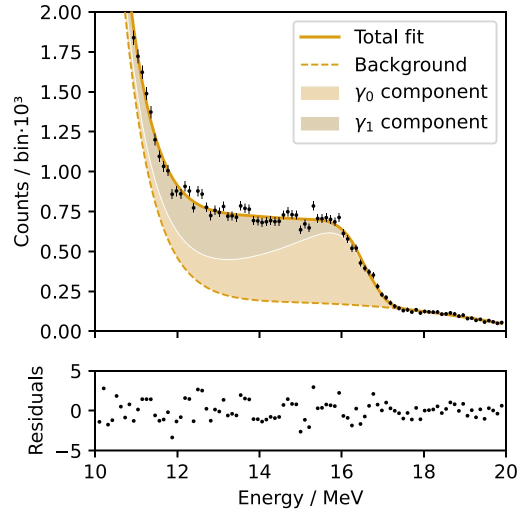

Figure 7. Fit on the sum spectrum of all selected discharges. The data are shown as black dots with their statistical errorbars. The fit components are shown as orange lines (solid for the total fit, dashed for the background. The contribution of γ_0 and γ_1 are shown separately as the two filled areas. The normalised residuals are presented in the bottom section.

5. Rescaling factors

With the absolute number of events at the detector at hand, the total DT gamma-ray yield could be determined by estimating the transport, attenuation and efficiency factors.

This implied to go through four steps: (1) measure the plasma DT gamma-ray emission profile, (2) describe the gamma-rays transport from the source to the detector front face, (3) quantify the attenuation due to the objects present along the beamline and (4) asses the detector absolute efficiency.

5.1. Gamma-rays emission profile

Since both 14 MeV neutrons and DT gamma-rays are emitted from the same reactants, the DT gamma-ray emission was considered to retain the same spatial emission distribution of the 14 MeV neutrons, under the assumption that the gamma-to-neutron branching ratio does not depend on the energy of the reactants. In fact, at the energies achieved at JET in the analysed discharges [26], DT reactions are strongly dominated by the ^{5}He second excited state resonance [18, 50, 51]. Furthermore, toroidal symmetry was assumed, allowing to only seek for spatial information in a poloidal section of the tokamak.

JET was provided both with neutron and gamma-ray camera diagnostics [52]. Because of the too high particle fluxes, though, the gamma-ray camera could not provide data for the whole duration of the DTE2 campaign. This made it necessary to use the neutron camera instead and make the previously mentioned assumption.

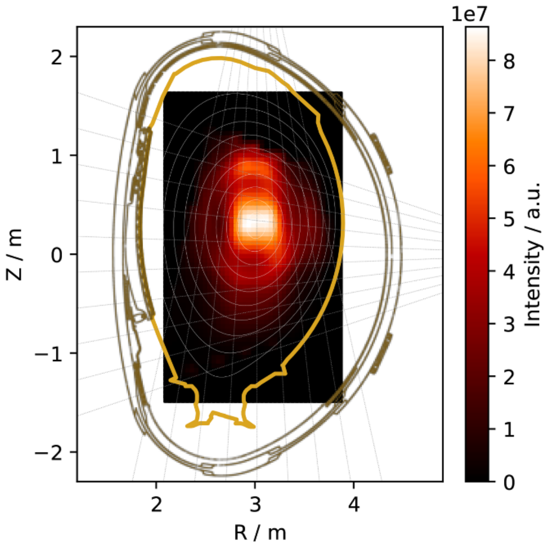

Figure 8. Tomographic reconstruction of the DT emission profile of JPN 99 740 based on the JET neutron camera data. The JET poloidal section is shown overlaied together with the 19 neutron camera lines of sight and some magnetic equilibrium surfaces.

The JET neutron camera is a diagnostic made of 19 NE213 liquid scintillator detectors (usually referred to as channels), all lying on the same plane and divided into 10 channels in the horizontal camera and 9 channels in the vertical one [53]. Each detector collects a neutron PHS evolving in time. For each analysed discharge, the events of each channel were integrated both in energy (with a lower energy threshold to discard scattered neutrons) and time (in the TGRS parsed time window), obtaining an array of 19 neutron yields divided into a vertical and an horizontal profile.

Then, a tomographic inversion was performed on the data to obtain the emission distribution in a poloidal section of the vessel. The maximum likelihood-expectation maximisation method was used to perform the inversion. In this algorithm, the result is computed by an iterative formula which, starting from the reconstructed profile and transporting the emission to the camera detectors, aims to reproduce the measured data as closely as possible. The procedure is described in [54] in detail. Information on the magnetic equilibrium are also embedded by means of a moving window average of the signal over the magnetic flux surface. In this work, the smoothing was applied every 2 iterations. The result was computed in a 40×70 pixels emission matrix, in which every pixel has an area of about 20 cm^2. An example is shown in figure 8.

5.2. Gamma-rays transport

Once the source was obtained, the probability for a gamma-ray born in the plasma according to that spatial distribution to reach the detector had to be computed. This probability will be referred to as the transport factor T. In principle, the plasma profile changes during a single discharge and should be determined at small temporal steps but, because of the too low signal in the PHS, it was necessary to integrate the PHS over large time windows and a single factor T was associated to each spectrum.

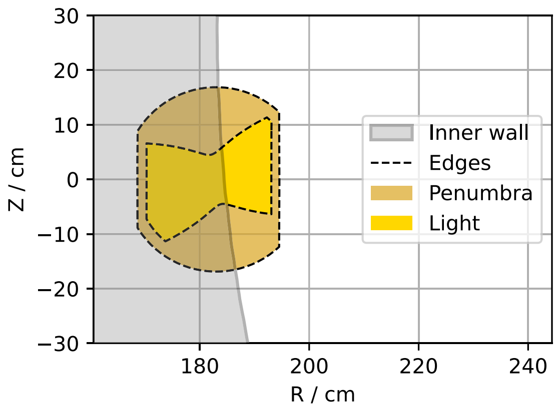

Figure 9. section of the tangential gamma-ray spectrometer line of sight. The section is shown at the tangent point with the inner vessel walls. At this point, the LoS is partially shielded by the vessel itself, as represented by the gray area.

Since an absolute measurement was to be performed, it was necessary to characterise the geometry as best as possible. From the detector to the plasma, these were the objects present along the LoS: the LiH attenuator (composed of LiH discs and steel splitters), the KX1 x-ray diagnostic [55–57], the concrete bioshield with its rectangular hole for the beamline, a vacuum-window made of steel and beryllium, the port at the vessel entrance, which partially covered the LoS, and the central column (which played a collimator role for the plasma source points in the second half of the vessel). From the bioshield to the vessel port, the LoS is contained inside a 12.2 cm radius inconel cylinder.

A code—named Linalytic—was implemented in Python in order to compute the optical transport of the gamma-rays. No attenuating effects were included, hence all attenuators (namely: LiH attenuator, x-ray diagnostic and vacuum-window) were removed, while the collimators were assumed to be completely opaque to gamma-rays. The fraction between the total emitted DT gamma-rays and the number of gamma-rays reaching the detector front face represent the T transport factor.

For each emission matrix pixel, the code constructs a toroidal ring centered in the pixel center and divided into a certain number of segments: the further the ring from the inner vessel, the higher the number of segments. For each segment, the probability of a particle born in its center to reach the detector was computed quasi-analytically.

This means that the probability within the light region of the ring was computed as the solution of an integral. For the penumbra regions, the probability was computed numerically, intersecting the projections of the collimators onto the detector plane with the detector front surface itself. At last, the average probability in each ring was computed. All details about this code are given in [39]. Among other functionalities, Linalytic can show the section of the LoS at the tangent point with the inner vessel. The plot is shown in figure 9. As can be observed,

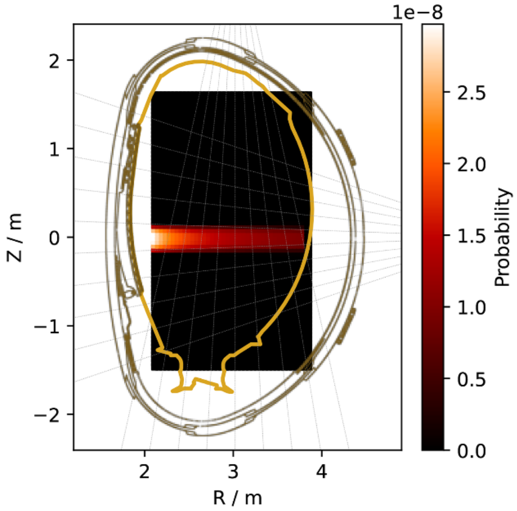

Figure 10. Tangential gamma-ray spectrometer transport matrix. Each entry contains the probability for a particle born in the toroidal voxel passing through that pixel to reach the detector front face. The JET poloidal section is shown overlaied together with the 19 neutron camera lines of sight.

the section is far from being circular because of all the collimating objects presents along the beamline.

As a result, a transport matrix is obtained, whose entries contain the probability for a gamma-ray born in the toroidal ring passing through that point to reach the detector front face. Its plot is shown in figure 10. The transport factor T is then computed as the weighted average of all the probabilities as:

$$T = \frac{\sum_i p_i e_i V_i}{\sum_i e_i V_i}$$

where i runs over the pixels, p_i are the transport matrix probabilities, e_i the emission matrix entries and V_i are the volumes of the toroidal voxels.

The transport was computed also with a MC simulation performed with the MCNP platform for two reference discharges (JPN 99 560 and JPN 99 608, selected as those with the most different plasma emission profiles), in order to benchmark the result. The MC simulation included both the official, complete geometry of the JET vessel and the detailed description of the spectrometer and its beamline. For the comparison, in MCNP all the attenuators were removed and all remaining objects were set to be completely opaque to the particles. This led to a discrepancy below 1% in T between the two approaches. This has proven the collimating objects implemented in Linalytic to be representative of the signal collimation. At last, according to MCNP, the gamma-ray signal increases only by 5.4% when the not-complete opacity of the collimators is taken into account.

The transport factors computed with Linalytic for all the analysed discharges follow a normal-like distribution centered at $2.271 \cdot 10^{-9}$, with a 2.45% standard deviation. This deviation was used as an uncertainty representative of the inaccuracies in the neutron camera measurements and tomographic inversion. Each PHS was used in combination with its emission profile transport factor.

In order to associate an uncertainty to the transport factor parameter, beside this Gaussian width, an other source of uncertainty was quantified by varying the toonable Linalytic parameters and MCNP collimators geometry within their relative uncertainty, obtaining a further $\sim$4.5% variation on T. Together, these uncertainties result in a total 5.12% uncertainty on T.

5.3. Gamma-rays attenuation

During the DTE2, as stated before, an average flux of about 10^{10} particles per second was expected at the detector, with about 10^5 times more neutrons than gamma-rays. Given the detector unitary efficiency to both kind of particles, the neutron-to-gamma-ray ratio would have remained the same also in the output spectrum, leaving the gamma-ray signal overwhelmed by the neutron induced background. Among other possible attenuators, LiH was the one which better suited the purpose of reducing the neutron flux, leaving the gamma-ray flux less affected as possible: the employed 93 cm of LiH attenuator reduced the neutron flux by a factor of $3.89 \cdot 10^{-4}$ and the gamma-ray flux of only 0.469.

MCNP was employed to compute the attenuation factor A, which includes the attenuation of all materials within the LoS together with the scattered gamma-rays component (less than 1%). Since the interaction with the materials depends on the energies of the particles at stake, two attenuation factors were computed by integrating in the RoI: $A_0 = 0.140(6)$ for γ_0 and $A_1 = 0.116(3)$ for γ_1, after having checked that their differences among different emission profiles was negligible (<0.7%).

The uncertainties associated to the attenuator factor were computed by increasing and decreasing the thickness of the steel slabs encapsulating the LiH attenuator by 0.4 mm.

5.4. Gamma-rays detection

As mentioned in section 2, $LaBr_3$ scintillation crystals manifest an intrinsic activity up to 3 MeV because of the ^{138}La isotope and ^{227}Ac contaminations. The main feature of the intrinsic spectrum is a composed peak centered at about 1470 keV, resulting from the electron capture of ^{138}La into ^{138}Ba, which is the isotope main decay channel, with a 65.2% branching ratio [58]. Since ^{138}La has an half life of $1.05 \cdot 10^{11}$ years, it is possible to consider its activity a constant and use this peak as a reference. Based on the natural abundance of this lanthanum isotope, its half life and the crystalline structure of $LaBr_3$, a direct relationship is present between the crystal volume and this peak intensity.

A novel technique was purposely developed to exploit this relation in order to infer a $LaBr_3$ crystal effective volume. By matching its activity with MC simulations of the crystal itself, it is possible to determine its volume, which is used in turn in input to further MC simulations to extrapolate the detection efficiency at higher gamma-ray energies. For the TGRS, the volume resulted compatible with the nominal value provided by the manufacturer within 0.07%. The technique and its validation are given in detail in [39].

For this work, an MCNP simulation was run including all the objects along the LoS in order to include alterations in the gamma-rays energy distribution from their emission to the detection. The spectrum of the energy deposited in the crystal per unitary source particle entering its front face was obtained as the simulation output. Given that the counts C are integrated between 12 and 17 MeV, also the detection efficiency had to be integrated in the same RoI leading to two efficiency factors: $\varepsilon_0 = 0.757$ for γ_0 and $\varepsilon_1 = 0.490$ for γ_1. Also in this case, their differences among different emission profiles was proven to be completely negligible.

6. Results

With all needed parameters at hand, the total gamma-ray yield could be estimated for all analysed discharges. Because of the two possible channels, the formula in section 1 had to be slightly adjusted as:

$$Y = \frac{C}{T}\left(\frac{f_0}{A_0\varepsilon_0} + \frac{f_1}{A_1\varepsilon_1}\right)$$

where only C and T vary with different spectra. The average uncertainty obtained on the total gamma-ray yield was 22.3(7)%, with the main uncertainty contributions coming from the background (71.00%) and γ_1 (24.78%) fraction of events identifications [26]. Assuming that the gamma-to-neutron branching ratio did not vary within the energies at stake in these plasma discharges, a linear relation with the total 14 MeV neutron yield would have worked as a validation of these results.

As mentioned in section 1, JET is equipped with absolutely calibrated neutron monitors which can provide the total neutron yield with a nominal 7% uncertainty. As shown in figure 11, a linear relation was in fact observed between the measured DT gamma-ray yield and the absolute neutron-yield. Relative uncertainties on the neutron yield are taken to be the nominal ones, while uncertainties on the gamma-ray yield shown in the figure include all the estimated contributions. The linear correlation was estimated with the Pearson correlation coefficient ρ, which resulted to be $\rho = 0.983$.

Finally, the slope of the linear fit $(2.4(5)\cdot 10^{-5})$ corresponds to the gamma-to-neutron branching ratio of the DT reaction, resulting in the first measurement of this physical quantity in a magnetic confinement fusion reactor [26].

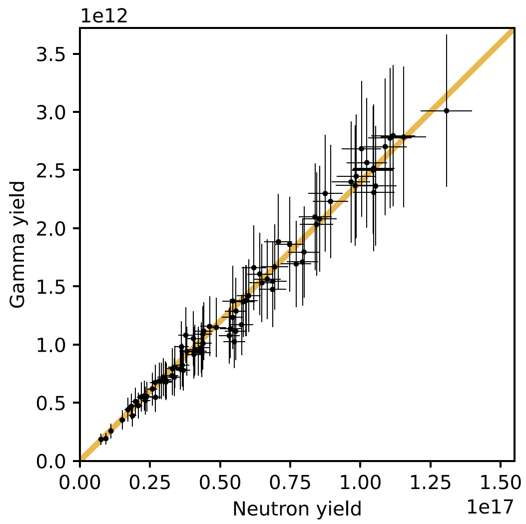

Figure 11. Total DT gamma-ray yield as a function of the total DT neutron yield. The slope of this linear relationship corresponds to the gamma-to-neutron branching ratio for the DT reaction.

7. Discussion

The results shown in section 6 have proven the feasibility to perform an absolute measurement of the total DT gamma-ray emission in a magnetic confined fusion plasma, paving the way for a novel direct method for the fusion yield assessment.

The average uncertainty on the total gamma-ray yield (22.3%) is larger compared to the standard technique nominal uncertainty achievable at JET (7%). Though, the neutronic method results from 40 years of experience, while the gamma-based one has been attempted for the first time. Furthermore, a pre-installed device was employed to perform this measurement, leaving room for improvements in the case of employment of dedicated, optimised diagnostics in future magnetic confined fusion devices.

Compared to the standard technique, this novel method is practically unaffected by scattered particles. This makes it independent on cross calibration with other diagnostics or heavy simulations of the whole tokamak, potentially reducing markedly the time required by the diagnostic calibration. Furthermore, there would be no need to repeat the calibration each time a variation happens in the tokamak surroundings.

At last, recent studies on the possibility to apply the method for fusion power assessment at ITER shown that measurements may be possible within the required uncertainty without a need to use information on the plasma emission profile [59], making the method completely independent on neutron measurements.

8. Conclusions

JET performed the DTE2 campaign at the end of 2021. Thanks to its unique capability of handling tritium, the first measurement of the total DT fusion reaction radiative emission could be performed.

This work presented the absolute measurement of the total gamma-ray emission of the DT fusion reaction for 96 DTE2 DT discharges. A single LoS gamma-ray spectrometer was employed for the purpose. Numerous challenges were addressed to pursue this goal: (1) the 10^5 times more intense neutron background was highly suppressed using a dedicated LiH attenuator, (2) the high event rate at the detector was handled with a stream-mode digitiser and ad-hoc implemented Python codes to handle pile-up, including degenerate pile-up, (3) the gamma-rays transport from the source to the detector was computed both with an analytical-numerical code and MC simulations, (4) the source emission profile was obtained through a tomographic inversion performed on the data collected with the JET neutron camera diagnostics, assuming that the gamma-ray emission had the same spatial distribution as neutrons.

The resulting total gamma-ray yields had an average 22.3% uncertainty and were validated by comparing them with the 14 MeV neutron yields provided by JET with a nominal 7% uncertainty, revealing an outstanding linear correlation with them (0.983 correlation coefficient).

In view of the potential use of this novel technique for inferring the total fusion power in future experiments, the uncertainties related both to the total gamma-ray yield and the gamma-to-neutron branching ratio will have to be reduced.

Experiments are planned at DT beam-target facilities in order to measure the branching ratio with a similar approach (employing both $LaBr_3$ detectors and LiH attenuator and also taking advantage of the time-of-flight technique). Regarding the achievable accuracy on the gamma-ray yield, studies are under consideration regarding the possibility to optimise the ITER radial gamma-ray set of spectrometers for measuring the fusion power in high power DT scenarios.

Acknowledgments

The authors thank Dr Vasili Kiptily for his fruitful comments on this manuscript.

This work has been carried out within the framework of the EUROfusion Consortium, funded by the European Union via the Euratom Research and Training Programme (Grant Agreement No. 101052200—EUROfusion). Views and opinions expressed are however those of the author(s) only and do not necessarily reflect those of the European Union or the European Commission. Neither the European Union nor the European Commission can be held responsible for them.

References

[1] Gauché F. and Garin P. 2007 Cadarache: the site for ITER *Revue Gén. Nucl.* **1** 80–84
[2] Tomabechi K. *et al* 1991 ITER conceptual design *Nucl. Fusion* **31** 1135
[3] Creely A. *et al* 2020 Overview of the SPARC tokamak *J. Plasma Phys.* **86** 865860502
[4] Kikuchi M. 2002 *Fusion Physics* (International Atomic Energy)
[5] Hendel H. *et al* 1990 In situ calibration of TFTR neutron detectors *Rev. Sci. Instrum.* **61** 1900–14
[6] Jarvis O., Sadler G., Van Belle P. and Elevant T. 1990 In-vessel calibration of the JET neutron monitors using a ^{252}Cf neutron source: difficulties experienced *Rev. Sci. Instrum.* **61** 3172–4
[7] Nishitani T., Takeuchi H., Kondoh T., Itoh T., Kuriyama M., Ikeda Y., Iguchi T. and Barnes C.W. 1992 Absolute calibration of the JT-60U neutron monitors using a ^{252}Cf neutron source *Rev. Sci. Instrum.* **63** 5270–8
[8] Johnson L., Barnes C.W., Duong H., Heidbrink W., Jassby D., Loughlin M., Roquemore A., Ruskov E. and Strachan J. 1995 Cross calibration of neutron detectors for deuterium-tritium operation in TFTR *Rev. Sci. Instrum.* **66** 894–6
[9] Hoek M., Nishitani T., Ikeda Y. and Morioka A. 1995 Neutron yield measurements by use of foil activation at JT-60U *Rev. Sci. Instrum.* **66** 885–7
[10] Bertalot L., Roquemore A., Loughlin M. and Esposito B. 1999 Calibration of the JET neutron activation system for DT operation *Rev. Sci. Instrum.* **70** 1137–40
[11] Syme D. *et al* 2014 Fusion yield measurements on JET and their calibration *Fusion Eng. Des.* **89** 2766–75
[12] Pu N., Nishitani T., Isobe M., Ogawa K., Kawase H., Tanaka T., Li S., Yoshihashi S. and Uritani A. 2017 In situ calibration of neutron activation system on the large helical device *Rev. Sci. Instrum.* **88** 11
[13] Batistoni P. *et al* 2017 14 MeV calibration of JET neutron detectors-phase 1: calibration and characterization of the neutron source *Nucl. Fusion* **58** 026012
[14] Batistoni P. *et al* 2018 14 MeV calibration of JET neutron detectors - phase 2: in-vessel calibration *Nucl. Fusion* **58** 106016
[15] Buss W., Wäffler H. and Ziegler B. 1963 Radiative capture of deuterons by ^{3}H *Phys. Lett.* **4** 198–9
[16] Bezotosnyi V., Zhmailo V., Surov L. and Shvetsov M. 1969 Cross section of the reaction T(d,γ)^{5}He with emission of 16.7 MeV γ quanta at 25–100 KeV deutron energy *Yadern. Fiz.* **10** 225–6
[17] Kosiara A. and Willard H. 1970 Gamma ray-neutron branching ratio in the triton-deutron reaction *Phys. Lett. B* **32** 99–100
[18] Cecil F. and Wilkinson F. 1984 Measurement of the ground-state gamma-ray branching ratio of the DT reaction at low energies *Phys. Rev. Lett.* **53** 767
[19] Morgan G., Lisowski P., Wender S., Brown R.E., Jarmie N., Wilkerson J.F. and Drake D. 1986 Measurement of the branching ratio ^{3}H(d,γ)/^{3}H(d, n) using thick tritium gas targets *Phys. Rev. C* **33** 1224
[20] Kammeraad J., Hall J., Sale K., Barnes C., Kellogg S. and Wang T. 1993 Measurement of the cross-section ratio ^{3}H(d,γ)^{5}He / ^{3}H(d,α)n at 100 KeV *Phys. Rev. C* **47** 29
[21] Balbes M., Riley J., Feldman G., Weller H. and Tilley D. 1994 Polarized deuteron capture by ^{3}He and ^{3}H at and above the fusion resonance region *Phys. Rev. C* **49** 912
[22] Parker C.E. 2016 The ^{3}H(d,γ) reaction and the ^{3}H(d,γ)/^{3}H(d,n) branching ratio for ec. m. $\leqslant$ 300 kev *PhD Dissertation* Ohio University
[23] Balbes M.J., Feldman G., Kramer L.H., Weller H.R. and Tilley D.R. 1991 Ground-state widths of ^{5}He and ^{5}Li determined in the ^{3}h(d,g)^{5}He and the ^{3}He(d,g)^{5}Li reactions *Phys. Rev. C* **43** 343–6
[24] Timofeyuk N.K., Bailey G.W. and Gilbert M.R. 2024 Modeling the γ spectrum from d-t collisions *Phys. Rev. C* **110** 014612
[25] Tilley D., Cheves C., Godwin J., Hale G., Hofmann H., Kelley J., Sheu C. and Weller H.R. 2002 Energy levels of light nuclei A = 5, 6, 7 *Nucl. Phys. A* **708** 3–163
[26] Dal Molin A. *et al* 2024 Measurement of the gamma-ray-to-neutron branching ratio for the deuterium-tritium reaction in magnetic confinement fusion plasmas *Phys. Rev. Lett.* **133** 055102
[27] Rebai M. *et al* 2024 First direct measurement of the spectrum emitted by the ^{3}H(^{2}H,γ)^{5}He reaction and assessment of the relative yield γ_1 to γ_0 *Phys. Rev. C* **110** 014625
[28] Maggi C.F. 2023 Overview of T and DT results in JET with ITER-like wall *Nucl. Fusion* **64** 112012
[29] Nocente M. *et al* 2022 Fusion product measurements by nuclear diagnostics in the joint european torus deuterium–tritium 2 campaign *Rev. Sci. Instrum.* **93** 093520

[30] Nocente M. *et al* 2021 A new tangential gamma-ray spectrometer for fast ion measurements in deuterium and deuterium–tritium plasmas of the joint European torus *Rev. Sci. Instrum.* **92** 043537
[31] Curuia M. *et al* 2017 Upgrade of the tangential gamma-ray spectrometer beam-line for JET DT experiments *Fusion Eng. Des.* **123** 749–53
[32] Kiptily V. *et al* 2024 Observation of alpha-particles in recent D–T experiments on JET *Nucl. Fusion* **64** 086059
[33] Maslov M. *et al* 2023 JET DT scenario with optimized non-thermal fusion *Nucl. Fusion* **63** 112002
[34] Tardocchi M., Nocente M. and Gorini G. 2013 Diagnosis of physical parameters of fast particles in high power fusion plasmas with high resolution neutron and gamma-ray spectroscopy *Plasma Phys. Control. Fusion* **55** 074014
[35] Marcer G. *et al* 2021 Study of a single line of sight gamma ray diagnostics for measurements of the absolute gamma ray emission from JET *J. Instrum.* **16** C12019
[36] Nocente M. *et al* 2010 Energy resolution of gamma-ray spectroscopy of JET plasmas with a $LaBr_3$ scintillator detector and digital data acquisition *Rev. Sci. Instrum.* **81** 10
[37] Knoll G.F. 2010 *Radiation Detection and Measurement* (Wiley)
[38] Saint-Gobain 2018 Physical properties of common inorganic scintillators (available at: https://luxiumsolutions.com/)
[39] Marcer G. 2025 A novel method for DT fusion power measurement in magnetic confinement plasmas based on the gamma ray emission from the D(T,^{5}He)γ reaction *PhD Dissertation* University of Milano-Bicocca
[40] Cazzaniga C., Nocente M., Tardocchi M., Rebai M., Pillon M., Camera F., Giaz A., Pellegri L. and Gorini G. 2015 Response of $LaBr_3$ (CE) scintillators to 14 MeV fusion neutrons *Nucl. Instrum. Methods Phys. Res. A* **778** 20–25
[41] Rigamonti D. *et al* 2022 Role of neutron attenuators for gamma-ray measurements in deuterium-tritium magnetic confinement plasmas *Rev. Sci. Instrum.* **93** 093515
[42] Dal Molin A. *et al* 2023 A new hard x-ray spectrometer for runaway electron measurements in tokamaks *Meas. Sci. Technol.* **34** 085501
[43] Rising M.E. *et al* 2023 MCNP® Code Version 6.3.0 Release Notes *Technical Report* LA-UR-22-33103 Los Alamos, NM, USA (available at: www.osti.gov/biblio/1909545)
[44] Van Rossum G. and Drake F.L. 2009 Python 3 Reference Manual CreateSpace, Scotts Valley, CA (available at: www.python.org/downloads/release/python-396/)
[45] Marcer G. *et al* 2022 A new dedicated signal processing system for gamma-ray spectrometers in high power deuterium-tritium plasma scenarios in tokamaks *Rev. Sci. Instrum.* **93** 093525
[46] Marcer G., Dal Molin A., Rebai M., Rigamonti D. and Tardocchi M. 2024 Degenerate pile-up correction in pulse height spectra from gamma-ray spectrometers *J. Fusion Energy* **43** 18
[47] Lane A.M. and Thomas R.G. 1958 R-matrix theory of nuclear reactions *Rev. Mod. Phys.* **30** 257–353
[48] Agostinelli S. *et al* 2003 Geant4 - A simulation toolkit *Nucl. Instrum. Methods Phys. Res. A* **506** 250–303
[49] Akaike H. 2011 Akaike's information criterion *International Encyclopedia of Statistical Science* pp 25–25
[50] Mohamed Z.L., Kim Y., Knauer J. and Rubery M. 2023 γ-to-neutron branching ratio for deuterium-tritium fusion determined using high-energy-density plasmas and a fused silica cherenkov detector *Phys. Rev. C* **107** 014606
[51] Kim Y. *et al* 2012 Determination of the deuterium-tritium branching ratio based on inertial confinement fusion implosions *Phys. Rev. C* **85** 061601
[52] Rigamonti D. *et al* 2018 The upgraded JET gamma-ray cameras based on high resolution/high count rate compact spectrometers *Rev. Sci. Instrum.* **89** 10
[53] Jarvis O., Adams J., Marcus F. and Sadler G. 1997 Neutron profile measurements in the joint European torus *Fusion Eng. Des.* **34** 59–66
[54] Panontin E. *et al* 2021 First spatially resolved measurements of the D-^{3}He α-particle source with the upgraded JET gamma-ray camera *Rev. Sci. Instrum.* **92** 053529
[55] Chernyshova M., Czarski T., Dominik W., Jakubowska K., Rzadkiewicz J., Scholz M., Pozniak K., Kasprowicz G. and Zabolotny W. 2014 Development of gem gas detectors for x-ray crystal spectrometry *J. Instrum.* **9** C03003
[56] Rzadkiewicz J. *et al* 2013 Design of T-GEM detectors for x-ray diagnostics on JET *Nucl. Instrum. Methods Phys. Res. A* **720** 36–38
[57] Shumack A. *et al* 2014 X-ray crystal spectrometer upgrade for ITER-like wall experiments at JET *Rev. Sci. Instrum.* **85** 11
[58] NIST 2021 Atomic weights and isotopic compositions for all elements (available at: https://physics.nist.gov/cgi-bin/Compositions/stand_alone.pl)
[59] Marcer G. *et al* 2024 Development of a measuring technique based on JET second DT campaign (DTE2) experience for assessing fusion power at ITER during DT operation using the radial gamma-ray spectrometer *Rev. Sci. Instrum.* **95** 8